Electrochimica Acta 549 (2026) 148023

Contents lists available at ScienceDirect

Electrochimica Acta

journal homepage: www.journals.elsevier.com/electrochimica-acta

Two *p*-tert-butylthiacalix[4]arene-supported bismuth cluster compounds for ultrahigh efficiency detection of trace-level Cd^{2+} and Pb^{2+}

Chang Liu [a], Tianlong Shan [b], Hongda Li [a], Sitong Wu [c], Meng Zhao [d], Guannan Wang [c,*], Rui Zhang [c,*]

[a] College of Criminal Science and Technology (College of Forensic Science), Criminal Investigation Police University of China, Shenyang 100854, PR China
[b] Organization of Personnel Division, Criminal Investigation Police University of China, Shenyang 100854, PR China
[c] Shenyang Key Laboratory of Medical Molecular Theranostic Probes in School of Pharmacy, School of Pharmacy, Shenyang Medical College, Shenyang, 110034, PR China
[d] School of Pharmacy, Shenyang Medical College, Shenyang, 110034, PR China

ARTICLE INFO

Keywords:
Heavy metal ions
Metal-organic Bi(III) clusters
Ultrahigh sensitivity
Mechanistic considerations

ABSTRACT

Heavy metal ions (HMIs) in the environment pose a significant threat to both environmental quality and human health. Consequently, monitoring HMIs concentrations is an essential yet challenging endeavor. Electrochemical sensing emerges as an effective method for detecting HMIs due to its high reliability and sensitivity. According to the hard/soft acid/base theory, porous metal-organic complexes containing S, O or N hybrid atoms provide the binding sites that facilitate the trapping of HMIs within cavities during the electrochemical deposition process, thereby enhancing detection sensitivity. In this study, we employed *p*-tert-butylthiacalix[4]arene ligands (H_4TC4A) to rationally design two Bi(III) clusters compounds: $[Bi_4(TC4A)_2(\mu_4\text{–}O)]\cdot 2NO_3\cdot 3DMF\cdot 3MeOH$ (**Bi_4-TC4A)** and $[Bi_8(TC4A)_5(en)_2(\mu_3\text{–}OH)_2(\mu_4\text{–}OH)_2]\cdot 5DMF\cdot 2MeOH$ **(Bi_8-TC4A)**. Furthermore, we constructed two Bi(III)-based electrochemical sensors, **Bi_4-TC4A/GCE** and **Bi_8-TC4A/GCE**, for the detection of Cd^{2+} and Pb^{2+} ions. Compared to **Bi_4-TC4A, Bi_8-TC4A** contains eight Bi(III) cations and five sulfur-containing $TC4A^{4-}$ ligands, which significantly enhance the enrichment and adsorption of HMIs for electrochemical sensing applications. Notably, the linear ranges for Cd^{2+} and Pb^{2+} on the **Bi_8-TC4A/GCE** were found to be 0.01–1.1 $mg{\cdot}L^{-1}$ and 0.01–1.4 $mg\ L^{-1}$ with the detection limits of 1.4 and 1.7 $\mu g\ L^{-1}$, respectively, which are lower than those specified by World Health Organization guidelines. This work offers valuable insights into utilizing well-designed Bi(III) cluster-based sensors for highly sensitive electrochemical detection of HMIs with low detection limits.

Environmental implication

Cd^{2+} and Pb^{2+} are highly toxic heavy metal pollutants that pose significant risks to the environment and human health. These contaminants can degrade soil and water quality, disrupt ecosystems, and accumulate in the food chain. In response to the urgent need for a rapid and accurate method for detecting HMIs in water and soil, this study has designed and synthesized two bismuth cluster compounds. These compounds effectively enrich HMIs by leveraging the cavity structure created by calixarene, enabling quantitative detection of Cd^{2+} and Pb^{2+}.

1. Introduction

In recent years, environmental issues have garnered significant attention [1,2]. Among these concerns, heavy metal ions (HMIs) are particularly problematic as they are non-biodegradable and tend to accumulate in living organisms, potentially leading to severe health complications and physiological disorders [3–5]. Therefore, HMIs are recognized as a major source of global biosphere pollution [6,7]. In this context, cadmium ions (Cd^{2+}), a highly toxic HMI, has fearful effects on kidney, liver, nerve system and cardiovascular health [8,9]. Lead ions (Pb^{2+}) represent another critical concern due to their detrimental effects on human health, which can cause damage on the circulatory system, nervous system and immune response even at low concentrations [10, 11]. Consequently, there is an urgent need for sensitive and selective

* Corresponding authors.
E-mail addresses: chemwangguannan@symc.edu.cn (G. Wang), ruizhang@symc.edu.cn (R. Zhang).

https://doi.org/10.1016/j.electacta.2025.148023
Received 16 November 2025; Received in revised form 14 December 2025; Accepted 15 December 2025
Available online 16 December 2025

detection methods for Cd^{2+} and Pb^{2+} that are both cost-effective and convenient [12–15]. Usually, traditionally employed analytical methods such as atomic absorption spectrometry (AAS) [16], atomic emission spectrometry (AES), and inductively coupled plasma-mass spectrometry (ICP-MS) have been utilized for the determination of HMIs [17,18], however, these methods often require expensive instrumentation and skilled personnel. In contrast, electrochemical square wave anodic stripping voltammetry (SWASV) offers advantages including straightforward operation, low cost, portability convenience, high sensitivity, and selectivity [19,20]. Thus, it becomes an alternative low-cost analytical approach for the electrochemical detection of Cd^{2+} and Pb^{2+}[21,22].

Bismuth (Bi)-based films serve as environmentally friendly electrode materials that facilitate the electroanalysis of HMIs due to their appealing characteristics such as low toxicity, ease of alloy formation with HMIs, and favorable electrochemical stripping behavior [23–25]. Compared to bismuth-based films, Bi nanoparticles (BiNPs) exhibit enhanced electrocatalytic activity attributed to their large specific surface areas along with abundant active sites [26]. Furthermore, Bi(III) cluster-based metal-organic compounds (MOCs) possess regular morphologies, diverse structures, tunable pore sizes, and rich active sites, which significantly enhance their applicability in this field [27–29]. The aforementioned structural characteristics promote the enrichment of HMIs to elevated levels, thereby realizing the electrochemical sensing of HMIs with high sensitivity [30,31]. Therefore, Bi(III) cluster-based MOCs are anticipated to represent a promising class of sensing materials for the detection of Cd^{2+} and Pb^{2+}.

In this work, a dumbbell-shaped tetranuclear Bi(III) cluster $[Bi_4(TC4A)_2(\mu_4\text{—}O)]\cdot 2NO_3\cdot 3DMF\cdot 3MeOH$ (**Bi_4-TC4A**) and a flower-shaped octanuclear Bi(III) cluster $[Bi_8(TC4A)_5(en)_2(\mu_3\text{—}OH)_2(\mu_4\text{—}OH)_2]\cdot 5DMF\cdot 2MeOH$ (**Bi_8-TC4A**) were synthesized by using the bowl-shaped *p*-tert-butylthiacalix[4]arene (H_4TC4A) ligands and Bi(III) cations. Considering their rich Bi(III) cations, bowl-shaped cavities, and the presence of Lewis soft base groups (compounds containing S, N, and O), these materials emerge as promising candidates for the detection of HMIs through the enrichment and adsorption of Cd^{2+} and Pb^{2+}. As a result, both Bi(III) clusters, **Bi_4-TC4A** and **Bi_8-TC4A**, were employed as electrochemical sensors for detecting Cd^{2+} and Pb^{2+} with wide concentration ranges. Notably, during simultaneous detection of these two HMIs, **Bi_8-TC4A** exhibited remarkably low limits of detection at 1.4 μg L^{-1} for Cd^{2+} and 1.7 μg $L^{-1}Pb^{2+}$. These values are much lower than the guideline thresholds established by World Health Organization (WHO). Furthermore, these limit values position our findings at the forefront among reported electrochemical sensors for Cd^{2+} and Pb^{2+} detection.

2. Experimental section

2.1. Synthesis of Bi_4-TC4A

$Bi(NO_3)_3\bullet 5H_2O$ (0.1 g, 0.2 mmol) and H_4TC4A (0.072 g, 0.1 mmol) were added to the mixed solution of DMF and MeOH (5:1, 6 mL). Then, ethylenediamine (en, 0.2 mL) was slowly added to the stirred solution. The resulting mixture was transferred into a Teflon-lined reactor (15 mL), heated at 130 °C for 3 days, and gradually cooled to room temperature. Green cubic crystals were obtained by filter and dried in air (~38 % yield based on H_4TC4A). Elemental analysis (%) Calcd for $[Bi_4(TC4A)_2(\mu_4\text{—}O)]\cdot 2NO_3\cdot 3DMF\cdot 3MeOH$: C 45.18, H 4.86, N 2.15, Found: C 45.31, H 4.62, N 2.33. IR (KBr, cm^{-1}): 2955(w), 1647(m), 1423(s), 1384(m), 1288(s), 1246(s), 1085(w), 873(w), 826(m), 730(m), 636(w), 611(w), 525(m).

2.2. Synthesis of Bi_8-TC4A

$Bi(NO_3)_3\bullet 5H_2O$ (0.1 g, 0.2 mmol) and H_4TC4A (0.08 g, 0.11 mmol) were added to the mixed solution of DMF and MeOH (1:1, 10 mL), and then ethylenediamine (en, 0.2 mL) and water (0.2 mL) were dropwise added to the stirring solution. After that, the mixture was put into a Teflon-lined reactor (15 mL) and heated at 130 °C for 3 days. Green rod-shaped crystals were achieved (~33 % yield based on H_4TC4A). Elemental analysis (%) Calcd for $[Bi_8(TC4A)_5(en)_2(\mu_3\text{—}OH)_2(\mu_4\text{—}OH)_2]\cdot 5DMF\cdot 2MeOH$: C 45.20, H 4.83, N 2.14, Found: C 46.26, H 4.30, N 2.43. IR (KBr, cm^{-1}): 2956(w), 2102(w), 1427(m), 1250(m), 1081(w), 878 (w), 819(w), 734(w), 497(s).

2.3. Fabrication of Bi(III) cluster based electrochemical sensors

Initially, a bare glassy carbon electrode (GCE) was polished using alumina slurries of 0.3 and 0.05 μm particle sizes, respectively, followed by thorough washing with alcohol and deionized water. The construction of the Bi(III) cluster-based electrochemical sensor proceeded as follows: the bulk Bi(III) cluster compounds were subjected to thorough grinding. Subsequently, 3.0 mg of the ground powder was dispersed in 1 mL of 0.5 wt % Nafion, followed by 15 min of ultrasonic treatment to yield a homogeneous suspension. Then, a 5 μL of the resulting 3.0 mg mL^{-1} Bi_8-TC4A suspension was drop-cast onto the surface of the freshly polished GCE. Finally, the modified electrode was dried under an infrared lamp (Scheme 1).

3. Results and discussion

3.1. Crystal structures of Bi_4-TC4A and Bi_8-TC4A

Single-crystal X-ray diffraction analysis reveals that **Bi_4-TC4A** presents a dumbbell-shaped structure centered on a tetranuclear Bi(III) cluster (Fig. 1a). Specifically, its structural framework consists of a central $[Bi_4(\mu_4\text{—}O)]^{10+}$ cluster capped by two $TC4A^{4-}$ anions (Fig. 1c). In the **Bi_4-TC4A** architecture, the Bi1 atom exhibits a coordination environment involving four phenoxy O atoms, two S atoms from two $TC4A^{4-}$ anions, and one bridging O atom derived from a coordinated water molecule (Fig. S1). The interatomic distances of $Bi1\text{—}Bi1^{\#1}$ and $Bi1\text{—}Bi1^{\#2}$ are measured as 3.215 Å and 3.189 Å, respectively, which fall within the range of reported Bi—Bi bonding lengths (2.947—3.219 Å) [32]. This observation allows the inference of metallic bonding interactions between adjacent Bi(III) cations.

Furthermore, by adjusting the solvent ratio, a new octanuclear cluster compound, **Bi_8-TC4A**, was successfully obtained. **Bi_8-TC4A** features a five-petal flower-shaped structure composed of a central $[Bi_8(\mu_3\text{—}OH)_2(\mu_4\text{—}OH)_2]^{20+}$ cluster and surrounded by five $TC4A^{4-}$ anions (Fig. 1b). Among the eight Bi(III) cations in this structure, Bi1 and Bi2 share an identical seven-coordinated environment, being surrounded by four O atoms, one S atom, and two bridging OH^- groups; Bi7 and Bi8 adopt the same nine-coordinated configuration, involving four O atoms, two S atoms, two N atoms, and one bridging OH^- group; While the remaining Bi3, Bi4, Bi5 and Bi6 each exhibit an octahedral coordination sphere, coordinated with four oxygen atoms, two sulfur atoms, and two OH^- groups (Fig. S2). To conveniently distinguish five $TC4A^{4-}$ anions in **Bi_8-TC4A**, the five anions are labeled as gray cup diagrams in Fig. 1d Finally, the crystallographic data and the selected bond lengths as well as angles of **Bi_4-TC4A** and **Bi_8-TC4A** are shown in Tables S1-S3.

3.2. Characterization of Bi_4-TC4A and Bi_8-TC4A

We selected DMF and MeOH as the optimal solvent system and employed ethylenediamine as the chelating agent to innovatively synthesize bismuth cluster crystals through the solvothermal method. The size and morphology of the resulting crystals under different solvent ratios were systematically characterized using optical microscope and scanning electron microscopy (SEM). Fig. 2a and b present the SEM images of the assembled bismuth cluster crystals, with the corresponding insets showing their optical micrographs. The **Bi_4-TC4A** compound, which consists of the $[Bi_4(\mu_4\text{-}O)]^{10+}$ cluster, forms diamond-shaped block

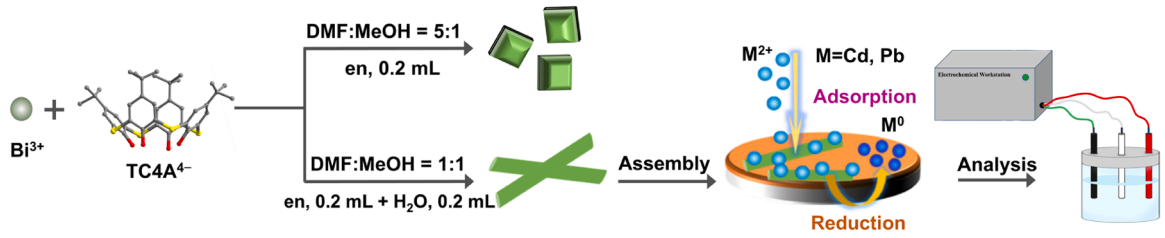

Scheme 1. Schematic representation of the synthesis process for **Bi_4-TC4A** and **Bi_8-TC4A**, along with the electrochemical detection of Cd^{2+} and Pb^{2+} on **Bi_8-TC4A/GCE** sensor (M = Cd, Pb).

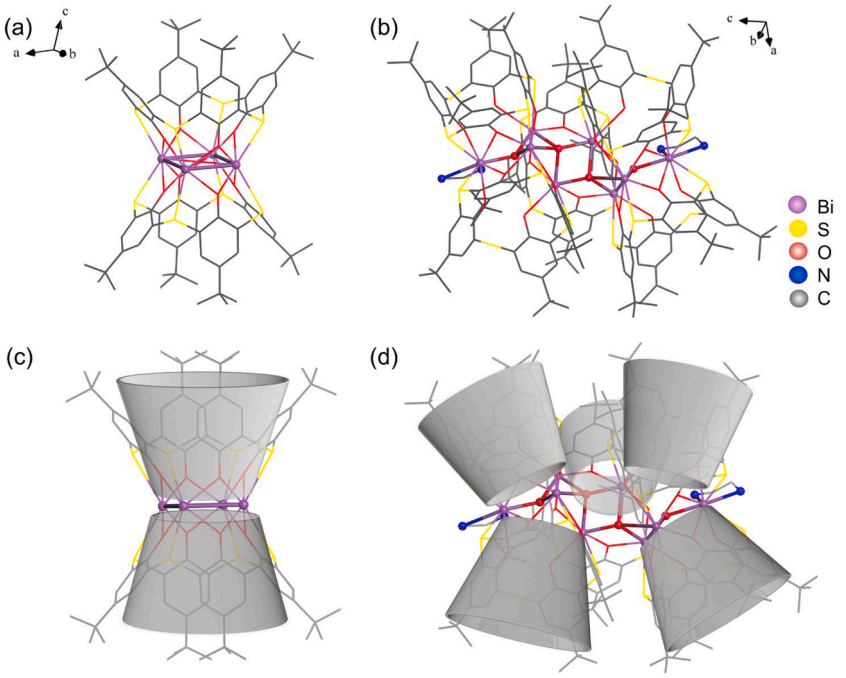

Fig. 1. Crystal structures of **Bi_4-TC4A** (a) and **Bi_8-TC4A** (b). Simplified coordination modes of **Bi_4-TC4A** (c) and **Bi_8-TC4A** (d).

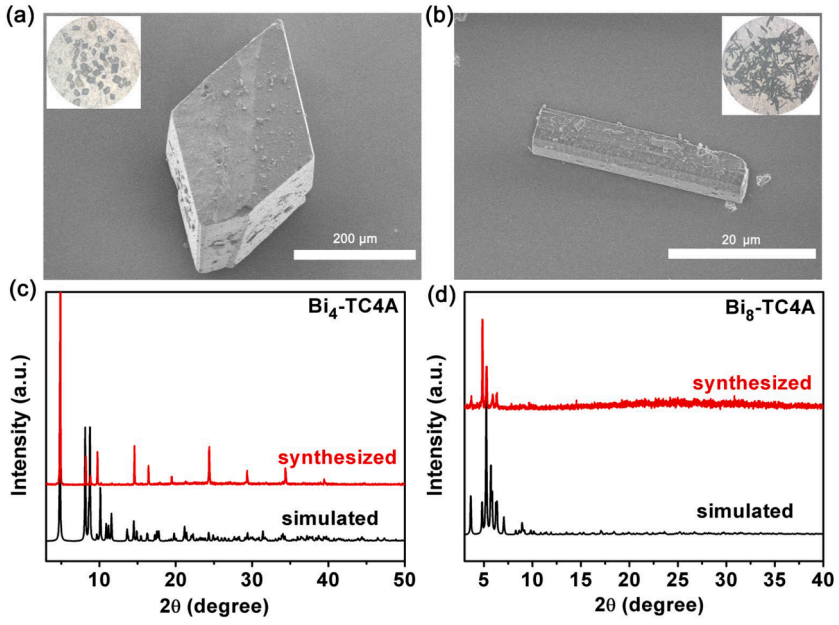

Fig. 2. SEM images of **Bi_4-TC4A** (a) and **Bi_8-TC4A** (b) (Insets: optical microscope photographs); The simulated and synthesized PXRD patterns for **Bi_4-TC4A** (c) and **Bi_8-TC4A** (d).

crystals measuring 200–400 μm in size. From the optical micrograph, these crystals are observed to be transparent with a pale green, displaying uniform thickness throughout (Fig. 2a). In contrast, **Bi_8-TC4A** compound, composed of the $[Bi_8(\mu_3\text{-}OH)_2(\mu_4\text{-}OH)_2]^{20+}$ cluster, crystallizes into dark green rod-like structures during slow solvent evaporation, with lengths ranging from 20 to 40 μm (Fig. 2b). Further, the phase purities of **Bi_4-TC4A** and **Bi_8-TC4A** were characterized by powder X-ray diffraction (PXRD) patterns (Fig. 2c and d). The PXRD patterns of the synthesized **Bi_4-TC4A** and **Bi_8-TC4A** matched well with the simulated ones, demonstrating the purity of the synthesized samples. To analyze the thermal stability of the two complexes, thermogravimetric (TG) curves of **Bi_4-TC4A** and **Bi_8-TC4A** were measured under nitrogen atmosphere from 25 to 800 °C (Fig. S3a and b). For **Bi_4-TC4A**, the weight loss before 299 °C can be ascribed to the release of three free DMF molecules and three free CH_3OH molecules. For **Bi_8-TC4A**, the weight loss before 312 °C corresponds to the release of five free DMF molecules and two free CH_3OH molecules.

Based on the results of the valence state calculations, **Bi_8-TC4A** is electrically neutral, whereas the framework of **Bi_4-TC4A** carries a positive charge. To achieve overall electrical neutrality in the compound, two positive charges from the framework were balanced by two NO_3^- anions, as evidenced by the absorption peak observed at approximately 1384 cm^{-1} in the FT-IR spectrum of **Bi_4-TC4A** (Fig. 3a) [33,34]. Furthermore, it is clear from the spectra that peaks at 1098 cm^{-1} and 556 cm^{-1} correspond to Bi–S and Bi–O bonds for both **Bi_4-TC4A** and **Bi_8-TC4A** (Fig. 3b) [35]. The broad peak around 500 cm^{-1} in **Bi_8-TC4A** arises from contributions of both Bi–N and Bi–O bonds [36]. Additionally, typical peaks located at 861 cm^{-1} are attributed to vibrations associated with Bi–O–Bi linkages [37]. Characteristic peaks found at 2960 cm^{-1}, 1656 cm^{-1}, 1450 cm^{-1}, and 1261 cm^{-1} can be assigned to C–H, C=C, $-CH_3$, and C–O groups present in calixarene respectively [38]. The presence of Bi(III) in **Bi_4-TC4A** and **Bi_8-TC4A** was confirmed through the analysis of the Bi 4f X-ray photoelectron spectroscopy (XPS) spectra (Figs. 3c and d and S4a and b). The spectrum for **Bi_4-TC4A** exhibited distinct peaks at binding energies of 164.1 eV and 158.8 eV, while that for **Bi_8-TC4A** displayed two unequal peaks at 163.8 eV and 158.5 eV, corresponding to the Bi $4f_{5/2}$ and $4f_{7/2}$ states, respectively. This observation indicates a separation of 5.3 eV, which is consistent with the oxidation state of Bi^{3+} [39]. Large specific surface areas and broad pore sizes are essential for effective adsorption applications [40,41]. The specific surface area and pore size distribution of the two compounds was examined using N_2 adsorption-desorption isotherms. As shown in Fig. 3e, the Brunauer-Emmett-Teller (BET) surface area for **Bi_8-TC4A** was calculated to be 141.13 $m^2\ g^{-1}$, significantly higher than that of **Bi_4-TC4A**, which measured of 91.94 $m^2\ g^{-1}$. Furthermore, the pore size distributions of **Bi_4-TC4A** and **Bi_8-TC4A** were analyzed from the desorption isotherm based on the Density Functional Theory (DFT) model, as illustrated in Fig. 3f. It is evident that both samples exhibit single-peak pore size distributions. The determined pore size was 3.55 nm for **Bi_4-TC4A** and 3.81 nm for **Bi_8-TC4A**.

3.3. *Electrochemical performance of Bi_4-TC4A/GCE and Bi_8-TC4A/GCE*

The electrochemical behavior of the electrolyte/electrode interface

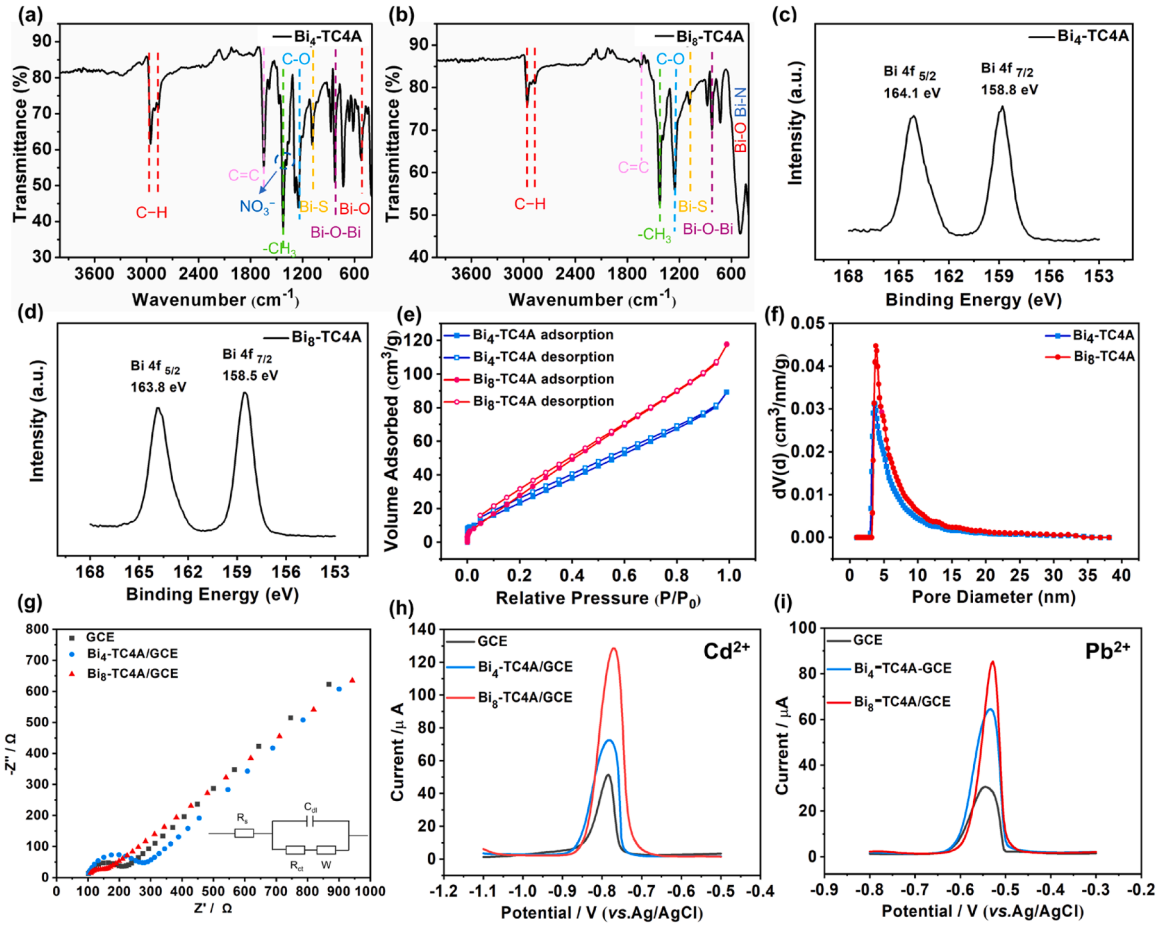

Fig. 3. FT-IR spectra of **Bi_4-TC4A** (a) and **Bi_8-TC4A** (b); XPS spectra of Bi 4f in **Bi_4-TC4A** (c) and **Bi_8-TC4A** (d); Plots of N_2 adsorption-desorption isotherms (e) and DFT pore size distributions (f) of **Bi_4-TC4A** and **Bi_8-TC4A**; Nyquist plots of bare GCE, **Bi_4-TC4A/GCE** and **Bi_8-TC4A/GCE** in the mixed solution of 10.0 mM $[Fe(CN)_6]^{3-}/[Fe(CN)_6]^{4-}$(1:1) and 0.1 M KCl (g); SWASV responses of different electrodes in the presence of 1.0 $mg{\cdot}L^{-1}$ Cd^{2+} (h) and 1.0 $mg{\cdot}L^{-1}$ Pb^{2+} (i) in 0.1 M NaAC—HAC (pH = 5.5) buffer solution.

and the reaction kinetics on the **Bi_4-TC4A/GCE** and **Bi_8-TC4A/GCE** sensing platforms were systematically investigated using electrochemical impedance spectroscopy (EIS) in a mixed solution containing 10.0 mM $[Fe(CN)_6]^{3-}$/$[Fe(CN)_6]^{4-}$ (1:1) and 0.1 M KCl. As illustrated in Fig. 3g, Nyquist plots for different electrodes were recorded and fitted to an equivalent electrical circuit for data analysis (inset in Fig. 3g). In the Nyquist plots, the high-frequency intercept corresponds to the uncompensated solution resistance (R_s), which was found to be comparable across all tested samples. The charge-transfer resistance (R_{ct}), reflecting the electrochemical reaction kinetics in the middle- to low-frequency range, was used as a key parameter for comparison; lower R_{ct} values indicate faster electron transfer kinetics [42]. Notably, both **Bi_4-TC4A** and **Bi_8-TC4A** exhibited significantly smaller semicircular arcs compared to those typically conventional metal–organic framework materials (ZIF, UiO, PCN and MIL) [13,43–45]. The obtained R_{ct} values were 96.1 Ω for the bare GCE, 148.5 Ω for **Bi_4-TC4A/GCE**, and 55.3 Ω for **Bi_8-TC4A/GCE**. These results clearly demonstrate that **Bi_8-TC4A/GCE** not only reduces the semicircular arc radius but also enhances electron transfer efficiency during the electrochemical process, suggesting its potential as a highly effective electrochemical sensing platform for metal ions detection. Moreover, SWASV technology was employed to evaluate and compare the electrochemical detection performances of Cd^{2+} (1.0 mg·L^{-1}) and Pb^{2+} (1.0 mg·L^{-1}) on the bare GCE, **Bi_4-TC4A/GCE**, and **Bi_8-TC4A/GCE**, respectively. Compared with the bare GCE, significantly enhanced current signals for both Cd^{2+} and Pb^{2+} were observed on **Bi_4-TC4A/GCE** and **Bi_8-TC4A/GCE** (Fig. 3h and i). Notably, the peak currents obtained on **Bi_8-TC$_4$A/GCE** were considerably higher than those on **Bi_4-TC4A/GCE**. This suggests that the abundant sulfur donor sites and structural cavities in **Bi_8-TC4A** facilitate the binding and accumulation of metal ions, thereby amplifying the electrochemical response. Consequently, **Bi_8-TC4A/GCE** exhibited more favorable sensing performance for detecting Cd^{2+} and Pb^{2+}.

3.4. Parameter optimization

During the electrochemical detection process, parameters such as electrolyte types, electrolyte pH value, deposition potential, and deposition time play crucial roles in influencing sensing performance [46,47]. Typically, these parameters affect the conversion rate and efficiency from M^{2+} (where M = Cd or Pb) to M^0 before being stripped back into solution [48]. The electrochemical detection method employed here involves the electro-deposition of M^{2+} followed by the anodic stripping of M^0 [49]. Consequently, we selected four buffer solutions including 0.2 M acetic acid buffer solution (ABS), 0.2 M phosphoric acid buffer solution (PBS), 0.2 M Britton-Robinson buffer solution (B-R), and 0.2 M NH_4Cl-HCl buffer solution for comparison the stripping peak currents of Cd^{2+} and Pb^{2+} at the **Bi_8-TC4A/GCE** (Fig. S5). Distinct discrepancies in the electrochemical responses were observed across the tested electrolyte systems. Specifically, in PBS and B-R buffer, the stripping peak current of Cd^{2+} was negligible, while that of Pb^{2+} was nearly undetectable. In the NH_4Cl-HCl buffer system, both Cd^{2+} and Pb^{2+} yielded measurable response currents, but the peak intensities were relatively low accompanied by irregular peak profiles. By contrast, well-resolved and high-intensity stripping peaks for both heavy metal ions were exclusively achieved in the ABS buffer solution. On this basis, ABS was identified as the optimal electrolyte for the subsequent detection of Cd^{2+} and Pb^{2+}. Subsequently, we investigated the effect of pH on peak current within a range of 4.0 to 6.0 (Fig. 4a and d). As pH values increased from 4.0 to 5.5, there was a significant enhancement in current signals due to strong adsorption and coordination of M^{2+} into **Bi_8-TC4A**. However, at a higher pH value of 6.0, signal attenuation may be attributed to the hydrolysis of Cd^{2+} and Pb^{2+} ions [13,50]. Therefore, optimal electrochemical detection for Cd^{2+} and Pb^{2+} occurred at a pH value of 5.5. The influence of deposition potentials on oxidative signals for Cd^{2+} and Pb^{2+} was examined by varying deposition potentials from −1.0 V to −1.4 V on **Bi_8-TC4A/GCE** (Fig. 4b and e). Stripping signals for both ions increased with more negative deposition potentials and the maximum peak currents were observed at −1.3 V, which was subsequently designated as the standard deposition potential for further tests. Similarly, we assessed how deposition time affected oxidation signals for Cd^{2+} and Pb^{2+}(Fig. 4c and f), maintaining a constant deposition potential at −1.3 V. The stripping currents for both Cd^{2+} and Pb^{2+} showed an increase with extended deposition times up to 300 s. Beyond this point, there was a notable decrease in current for Cd^{2+}, while that for

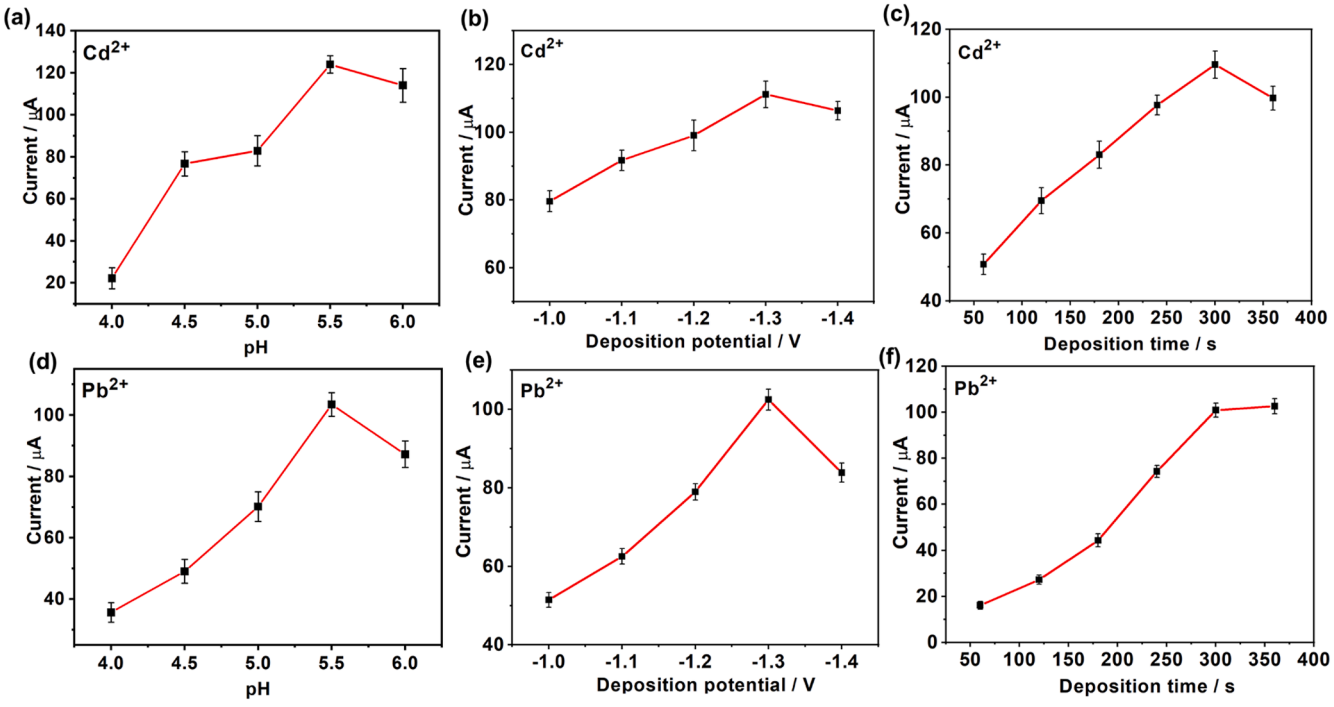

Fig. 4. Effect of the supporting electrolyte pH values (a, d), deposition potentials (b, e) and deposition time (c, f) on the current responses of 1.0 mg·L^{-1} Cd^{2+} and 1.0 mg·L^{-1} Pb^{2+} at **Bi_8-TC4A/GCE**.

Pb^{2+} remained stable. Consequently, a standard deposition time of 300 s would be utilized in subsequent electroanalytical studies.

3.5. Electrochemical determination of Cd^{2+} and Pb^{2+}

In this study, **Bi_8-TC4A/GCE** was used to monitor Cd^{2+} and Pb^{2+} under the optimal conditions with 0.1 M NaAC—HAC buffer solution (pH = 5.5). As illustrated in Fig. 5a and c, the anodic stripping peaks towards Cd^{2+} and Pb^{2+} appeared at around −0.80 V and −0.55 V, respectively. Obviously, the separation of the stripping potentials made it possible to detect Cd^{2+} and Pb^{2+} simultaneously in the mixed solutions. The oxidation peak currents of Cd^{2+} increased gradually with the raised Cd^{2+} concentrations. The resulting calibration data plots were found to be linearly proportional to the concentrations over the range of 0.01–1.1 mg·L^{-1}. Particularly, the relationship of the Cd^{2+} concentrations and peak current values could be expressed as I (μA) = 113.08 C (mg·L^{-1}) – 0.68, with a high-correlation coefficient (R^2) value of 0.9939 fitted from Fig. 5b The limit of detection (LOD) was 1.9 μg·L^{-1}, which is absolutely effective to identify Cd^{2+} within the maximum allowable value (0.003 mg·L^{-1}) set by World Health Organization (WHO) [51]. Similarly, the calibration curve for Pb^{2+} showed a good linear relationship in the concentration range of 0.01–1.4 mg·L^{-1} (Fig. 5d), corresponding to the regression equation of I (μA) = 87.54 C (mg·L^{-1}) – 2.37 (R^2 = 0.9924). The LOD was calculated to be 2.8 μg·L^{-1}, which is much lower than the guideline value (0.01 mg·L^{-1}) specified by WHO [52]. In the present study, the LOD was calculated following the formula LOD=3σ/b, where σ denotes the standard deviation of the peak currents derived from 11 replicate measurements in a blank NaAc-HAc buffer solution, and b corresponds to the slope of the calibration plot.

Finally, the electrochemical sensing performances of Cd^{2+} and Pb^{2+} were measured simultaneously under the optimized conditions on **Bi_8-TC4A/GCE**. Two well-defined peaks at around –0.80 V and –0.55 V were observed for Cd^{2+} and Pb^{2+}, respectively (Fig. 5e). As illustrated in Fig. 5f, the stripping currents were enhanced with the increased analyte concentrations. The good linear relationships between the stripping currents and the concentrations of Cd^{2+} and Pb^{2+} were observed in the detection range from 0.005 to 1.2 mg·L^{-1}, and linear equations are I(μA) = 108.40 C (mg·L^{-1}) + 2.94 (R^2 = 0.9917) for Cd^{2+} and I(μA) = 83.42 C (mg L^{-1}) + 0.78 (R^2 = 0.9983) for Pb^{2+}. Compared with other bi-based material or nanomaterial electrodes (Table S4), the designed **Bi_8-TC4A/GCE** sensor exhibited satisfactory detection results. Relative to the previously reported sensors, **Bi_8-TC4A/GCE** exhibited extremely

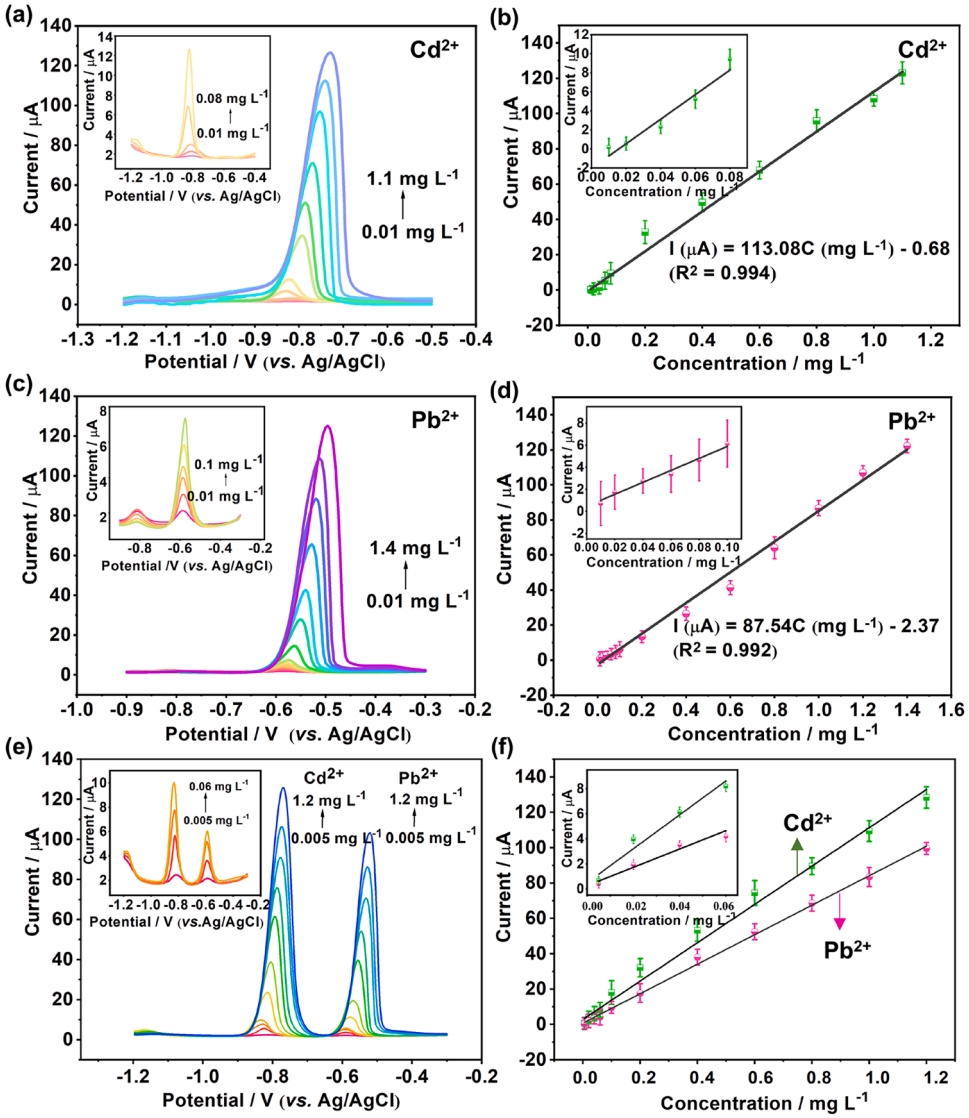

Fig. 5. Typical SWASV responses for Cd^{2+} and Pb^{2+} on **Bi_8-TC4A/GCE** (a, c) (Inset: the SWASV curves for low concentrations of Cd^{2+} or Pb^{2+}) and the corresponding linear calibration plots (b, d) (Inset: the magnifying linear calibration plots at low concentration of Cd^{2+} or Pb^{2+}); (e) SWASV responses for simultaneous detection of Cd^{2+} and Pb^{2+} over the concentration range from 0.005 to 1.2 mg·L^{-1}; (f) The corresponding calibration plots toward Cd^{2+} and Pb^{2+}, respectively.

wide linear ranges for the detection of Cd^{2+} and Pb^{2+}, which spanned three orders of magnitude. Particularly, the LOD values for Cd^{2+} and Pb^{2+} were 1.4 μg·L^{-1} and 1.7 μg·L^{-1}, respectively, which were at the upstream detection level in Cd^{2+} and Pb^{2+} sensors. Particularly, the LOD values are much lower than the standard drinking water ones from the WHO. More significantly, the constructed **Bi_8-TC4A/GCE** electrode is inexpensive and easy to fabricate than the known Bi film electrodes.

3.6. Mechanistic considerations

To get insights into the mechanism of first-class adsorption capacity and outstanding electrochemical performance to Cd^{2+} and Pb^{2+} on **Bi_8-TC4A/GCE**, we apply the DFT calculations to investigate the adsorption behaviors of Cd^{2+} and Pb^{2+} on **Bi_8-TC4A** surfaces focusing on both electronic structures and optimized chemical bond parameters. The analysis of the density of states (DOS) indicates that although the Bi orbital projected density of states (PDOS) of both **Bi_4-TC4A** and **Bi_8-TC4A** cross the Fermi level (E_F), there is a notable difference in their electronic density of states distribution at the E_F (Fig. 6a and b). **Bi_8-TC4A** shows a clear DOS peak at E_F, whereas the DOS for **Bi_4-TC4A** near E_F is approximately zero. This disparity in electronic structure accounts for the superior conductivity observed in **Bi_8-TC4A** compared to **Bi_4-TC4A** [53], which aligns well with results obtained from EIS tests. To further elucidate the electronic interactions between Cd^{2+} or Pb^{2+} ions and **Bi_8-TC4A** surfaces, we compared the partial PDOS before and after the adsorption of Cd^{2+} or Pb^{2+} at the most stable metal-top sites (Fig. 6c and d). For $Pb(H_2O)_4^{2+}$, it is noteworthy that the dominant peak of Pb orbitals is situated significantly above the E_F. Following adsorption on **Bi_8-TC4A** surfaces, the corresponding *s* and *p* orbitals exhibit a pronounced downshift towards the E_F, which results from substantial electron transfer from **Bi_8-TC4A** [54]. In examining **Bi_8-TC4A** surfaces, we observe a favorable alignment between S-3p orbitals and Pb-6 s orbitals. This observation substantiates the formation of Pb-S bonds due to chemisorption. Furthermore, overlapping p-p orbital interactions between Pb and S sites are also detected, reinforcing efficient electron transfer mechanisms. The effective coupling between s-p and p-p orbitals ensures robust formation of Pb-S bonds. Similarly, it has been confirmed that S atoms exert a comparable adsorption effect on Cd^{2+} ions. In addition, DFT calculations also indicate that the aromatic ring structure can serve as binding sites for Cd^{2+} and Pb^{2+} ions, facilitating their adsorption through the well-known cation•••π interaction. The optimized binding distances for the cation ··π interactions are presented in Fig. 6e–h, and the geometric parameters are detailed in Table 1. Considered that **Bi_8-TC4A** comprises five $TC4A^{4-}$ anions and $[Bi_8(\mu_3\text{—}OH)_2(\mu_4\text{—}OH)_2]^{20+}$ cations, one of the $TC4A^{4-}$ anions along with its directly connected atoms has been selected as the calculation model to enhance computational efficiency.

3.7. Reproducibility, storage stability and selectivity

To explore the reproducibility of **Bi_8-TC4A** modified electrode, five parallel experiments were conducted for the electrochemical detection of Cd^{2+} and Pb^{2+}. The SWASV responses for Cd^{2+} (1.0 mg·L^{-1}) and Pb^{2+} (1.0 mg·L^{-1}) on five **Bi_8-TC4A/GCE** electrodes are shown in Figs. 7a and S6a. It can be observed that the stripping currents on **Bi_8-TC4A/GCE** were nearly constant and the relative standard deviations (RSDs) were calculated to be 2.73 % and 4.63 % for Cd^{2+} and Pb^{2+}, respectively. These results demonstrated that **Bi_8-TC4A/GCE** featured good reproducibility for the electrochemical determination of Cd^{2+} and Pb^{2+}. To verify its storage stability, the **Bi_8-TC4A/GCE** sensor was employed for monitoring the concentrations of Cd^{2+} and Pb^{2+} every day continuously for a week (the electrode was stored at 4 °C when it was not used). Compared with its initial values, the peak currents of Cd^{2+} and Pb^{2+} did not decrease significantly, remaining 94.67 % and 92.77 % of the initial current values, respectively (Figs. 7b and S6b). Furthermore, interference ions, such as K^+, Na^+, Mg^{2+}, Zn^{2+}, Ca^{2+}, Co^{2+}, Mn^{2+}, Cr^{3+}, Fe^{3+} and Al^{3+}, were used to assess the selectivity of the electrochemical sensor. The concentration of interfering ions was 10 mg·L^{-1}, which was 10-fold higher than that of Cd^{2+} or Pb^{2+}. As illustrated in Fig. 7c, the addition of these interference ions did not lead to the obvious current value changes of Cd^{2+} and Pb^{2+}, demonstrating good selectivity of the sensing platform for the simultaneous detection of Cd^{2+} and Pb^{2+}.

3.8. Applications to lake water, soil and food samples

The applicability performance of the **Bi_8-TC4A/GCE** sensor was examined in real lake water, soil and food samples due to the presence of the unknown interfering substances during Cd^{2+} and Pb^{2+} detection. Before determination, lake water, soil leaching and orange juice solutions were filtered through a 0.22 μm membrane to remove the suspended solids, and then the actual samples were diluted with 0.2 M NaAc-HAc buffer solution (pH = 5.5) in a ratio of 1:9. The spinach samples were dipped with cotton swabs on their surfaces and then added to the 0.2 M NaAc-HAc buffer solution (pH = 5.5). SWASV

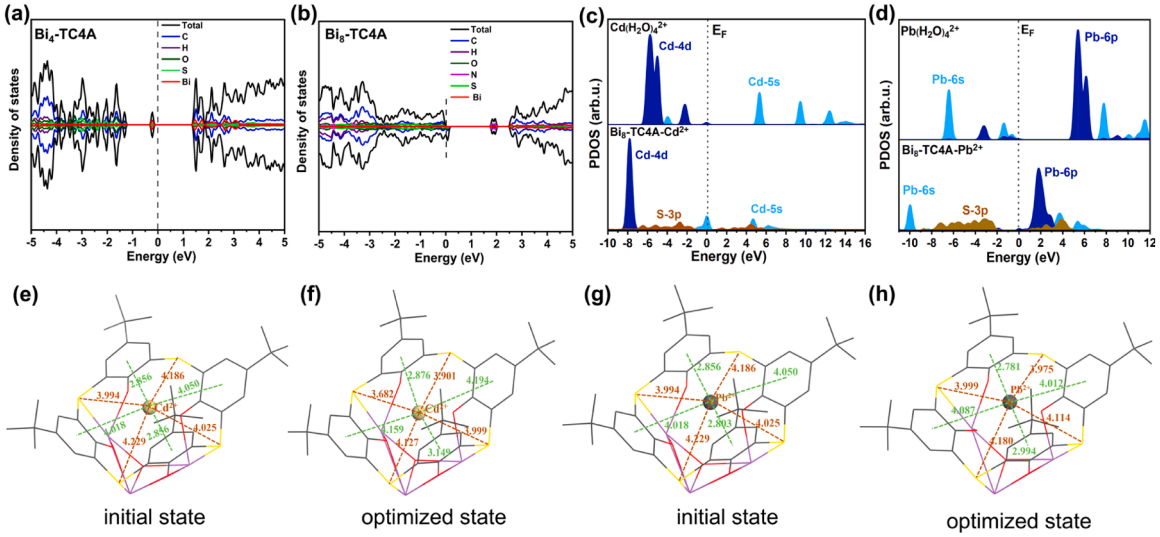

Fig. 6. Calculated DOS for (a) **Bi_4-TC4A** and (b) **Bi_8-TC4A**; The partial PDOS of comparisons for Cd^{2+} (c) or Pb^{2+} (d) adsorptions on **Bi_8-TC4A** (S-3p represent the 3p orbitals of S atoms of **Bi_8-TC4A**, $Pb(H_2O)_4^{2+}$ represents hydrated lead ion, $Cd(H_2O)_4^{2+}$ represents hydrated cadmium ion); Partial **Bi_8-TC4A** computational model structure (initial and optimized state for adsorption of Cd^{2+} and Pb^{2+}) and cation···π, Cd-S, and Pb-S binding distances (e-h).

Table 1
Optimized cation···π and M − S binding distances.

M^{2+}	Cation··π binding distances (Å)				M − S binding distances (Å)			
Cd^{2}	2.876	4.194	3.149	4.159	3.901	3.999	4.127	3.682
Pb^{2+}	2.781	4.012	2.994	4.087	3.975	4.114	4.180	3.999

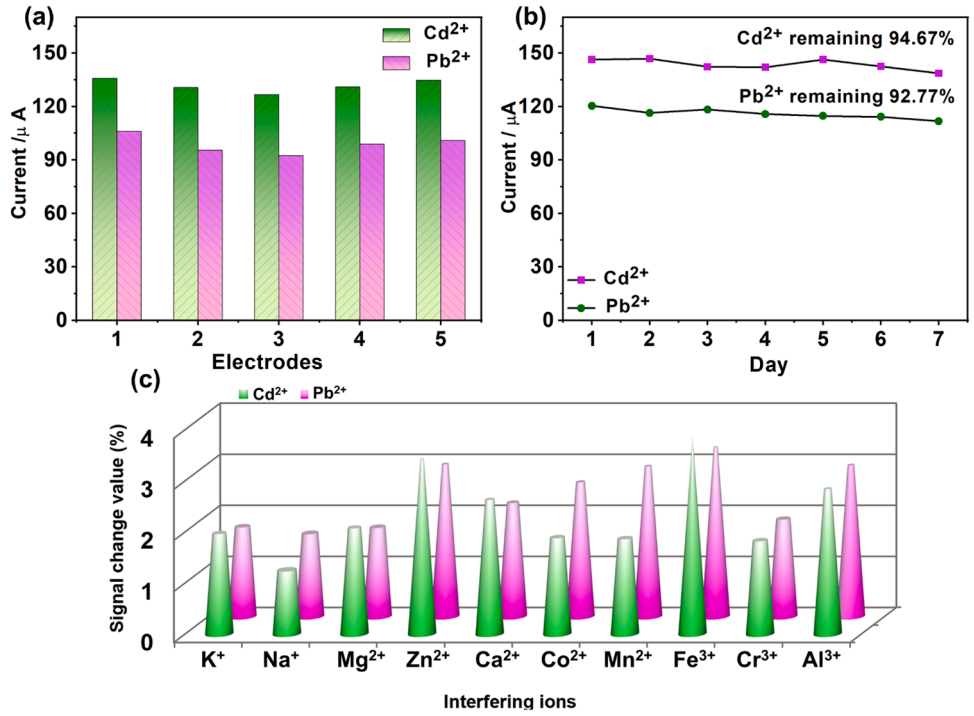

Fig. 7. (a) The repeatability of **Bi_8-TC4A/GCE** by the parallel determination of Cd^{2+} ($mg{\cdot}L^{-1}$) and Pb^{2+} ($mg{\cdot}L^{-1}$) for five times; (b) The stability of **Bi_8-TC4A/GCE** by the measurement of Cd^{2+} ($mg{\cdot}L^{-1}$) and Pb^{2+} ($mg{\cdot}L^{-1}$) every day for one week; (c) Percentage of current signal change values for Cd^{2+} ($mg{\cdot}L^{-1}$) and Pb^{2+} ($mg{\cdot}L^{-1}$) on the as-prepared **Bi_8-TC4A/GCE** in 0.1 M NaAc-HAc (pH = 5.5) containing 10-fold interfering ions.

determination results displayed that no current responses of Cd^{2+} and Pb^{2+} were observed in these samples, indicating that the concentrations of the target analytes were extremely low or no target analytes in the real samples. With the standard addition method, the practical application of the proposed sensor was evaluated by recovery determination of the spiked metal ion in water samples, and the results are listed in Table 2. It can be seen that the calculated average recovery ranged from 95.4 % to 104.0 %, demonstrating that the **Bi_8-TC4A/GCE** electrode featured a good potential application for detection of Cd^{2+} and Pb^{2+} in practical environment and food samples.

4. Conclusions

In summary, two novel Bi(III) clusters, **Bi_4-TC4A** and **Bi_8-TC4A**, were successfully synthesized by varying the ratio of the reaction solvents. **Bi_4-TC4A** exhibits a dumbbell-shaped tetranuclear structure, whereas **Bi_8-TC4A** features a flower-shaped octanuclear configuration. Compared to **Bi_4-TC4A, Bi_8-TC4A** demonstrates superior electrical conductivity and enhanced capacity for HMIs enrichment, rendering it an ideal candidate as an electrode modification material for the detection of Cd^{2+} and Pb^{2+}. During electrochemical assessments of Cd^{2+} and Pb^{2+}, the **Bi_8-TC4A/GCE** exhibited remarkable sensitivity, selectivity and stability. Notably, it holds significant potential for detecting Cd^{2+} and Pb^{2+} in real soil, lake water and food samples. The LODs for Cd^{2+} and Pb^{2+}, determined using the **Bi_8-TC4A/GCE** system, are substantially lower than the guideline values established by WHO. The successful integration of calix[4]arene into both Bi(III)-based clusters provides an effective approach to enhance HMIs detection capabilities.

Table 2
Separate detection of Cd^{2+} and Pb^{2+} added in lake water and soil leaching solutions by SWASV.

Analytes	Samples	Orginal	Added (mg L^{-1})	Found [a] (mg L^{-1})	Recovery (%)	R.S.D (n = 3; %)
Cd^{2+}	Lake water	ND	0.050	0.048	96.0	3.11
			0.500	0.482	96.4	2.52
	Soil	ND	0.050	0.051	102.0	2.88
			0.500	0.503	100.6	1.15
Pb^{2+}	Lake water	ND	0.050	0.052	104.0	2.48
			0.500	0.511	102.2	3.47
	Soil	ND	0.050	0.049	98.0	2.23
			0.500	0.520	104.0	1.98
Cd^{2+}	spinach	ND	0.050	0.048	96.0	2.54
			0.500	0.477	95.4	2.88
	orange juice	ND	0.050	0.049	98.0	3.12
			0.500	0.515	103.0	2.98
Pb^{2}	spinach	ND	0.050	0.052	104.0	1.76
			0.500	0.502	100.4	3.32
	orange juice	ND	0.050	0.049	98.0	1.88
			0.500	0.518	103.6	2.35

ND: no detection signal of analyte
[a] the average of the three repeated tests.

CRediT authorship contribution statement

Chang Liu: Writing – original draft, Visualization, Data curation, Conceptualization. **Tianlong Shan:** Writing – review & editing, Validation. **Hongda Li:** Project administration, Funding acquisition. **Sitong Wu:** Writing – review & editing, Funding acquisition. **Meng Zhao:** Writing – review & editing. **Guannan Wang:** Methodology, Funding acquisition. **Rui Zhang:** Methodology, Funding acquisition, Conceptualization.

Declaration of competing interest

The authors declare that they have no known competing financial interests or personal relationships that could have appeared to influence the work reported in this paper.

Acknowledgments

This work was financially supported by Applied Basic Research Foundation of Liaoning Province, China (2025JH2/101330098), Outstanding Young and Middle-aged Scientists Foundation of Shenyang City, China (RC240575), Natural Science Foundation of Liaoning Province (2025-BS-0251), National Natural Science Foundation of China (no 21804140), Science and Technology of the Ministry of Public Security of the People's Republic of China (no 2024yy49), General Program of Natural Science Foundation of Liaoning Province (2025-MS-295), Natural Science Foundation of Liaoning Province (2023-BSBA-293) and Basic Scientific Research Project of Liaoning Provincial Department of Education (grant no LJ212510175006).

Supplementary materials

Supplementary material associated with this article can be found, in the online version, at doi:10.1016/j.electacta.2025.148023.

Data availability

Data will be made available on request.

References

[1] H. Tang, W. Chang, H. Xue, C. Xu, Z. Li, H. Liu, C. Xing, G. Liu, X. Liu, H. Wang, J. Wang, Engineered DNA molecular machine for ultrasensitive detection of environmental lead pollution, J. Hazard. Mater. 459 (2023) 132306.
[2] K. Wang, X. Meng, X. Yan, K. Fan, Nanozyme-based point-of-care testing: revolutionizing environmental pollutant detection with high efficiency and low cost, Nano Today 54 (2024) 102145.
[3] R. Wu, Z. Wang, Y. Fu, J. Jiang, Y.-C. Chen, T. Liu, High-sensitive hydrogel optofluidic microcavities for heavy metal ion detection, ACS Sens. 10 (2025) 2330–2338.
[4] Y. Tian, J. Liu, J. Qiao, F. Ge, Y. Yang, Q. Zhang, Advancements in electrochemical sensing technology for heavy metal ions detection, Food Chem. X 25 (2025) 102204.
[5] M.A.M. Hasan, W. Qian, J. Wang, H. Wu, Y. Wang, Y. Yang, Eco-friendly and low-cost heavy metal ion detection *via* droplet-generated triboelectricity, Nano Energy 131 (2025) 110320.
[6] J. Guo, J. Li, X. Xing, W. Xiong, H. Li, Development of MOF-derived Co_3O_4 microspheres composed of fiber stacks for simultaneous electrochemical detection of Pb^{2+} and Cu^{2+}, Microchim. Acta 191 (2024) 542.
[7] Y. Wang, Z. Nie, X. Li, Y. Zhao, H. Wang, Highly sensitive and selective electrochemical sensor based on porous graphitic carbon nitride/$CoMn_2O_4$ nanocomposite toward heavy metal ions, Sens. Actuat. B Chem. 346 (2021) 130539.
[8] H. Liu, Y. Zhou, J. Xu, L. Ding, C. Liao, T. Wang, H. Zhou, G. Zhou, Multiplex detection of Cd^{2+}, Hg^{2+}, glutathione, and ascorbic acid using $NaYF_4$: yb, Er@ $NaYF_4$ core-shell upconversion nanoparticles and trithiocyanuric acid-modified gold nanoparticles, ACS Appl. Nano Mater. 8 (2025) 8054–8065.
[9] X. Guo, S. Feng, Y. Peng, B. Li, J. Zhao, H. Xu, X. Meng, W. Zhai, H. Pang, Emerging insights into the application of metal-organic framework (MOF)-based materials for electrochemical heavy metal ion detection, Food Chem. 463 (2025) 141387.
[10] Y. Zhang, H. Wei, Y. Li, Z. Shang, R. Zhang, Z. Zhang, Q. Meng, An azacrown ether-based near-infrared fluorescent probe for the detection of Pb^{2+} and its applications in food, environmental water, plant and animal samples, Anal. Chim. Acta 1351 (2025) 343882.
[11] J. Xu, Y. Li, F. Wang, X. Luo, W. Zhang, Y. Lyu, H. Yang, R. Cai, W. Tan, On-demand controlled bidirectional DNAzyme path for ultra-sensitive heavy metal ion detection, Chem. Sci. 15 (2024) 18170–18178.
[12] L. Ma, W.-Y. Pei, J. Yang, J.-F. Ma, A new thiacalix[4]arene-based metal-organic framework as an efficient electrochemical sensor for trace detection of Cd^{2+} and Pb^{2+}, Food Chem. 441 (2024) 138352.
[13] M. Lu, Y. Deng, Y. Luo, J. Lv, T. Li, J. Xu, S.-W. Chen, J. Wang, Graphene aerogel-metal-organic framework-based electrochemical method for simultaneous detection of multiple heavy-metal ions, Anal. Chem. 91 (2018) 888–895.
[14] L. Ma, X. Zhang, M. Ikram, M. Ullah, H. Wu, K. Shi, Controllable synthesis of an intercalated ZIF-67/EG structure for the detection of ultratrace Cd^{2+}, Cu^{2+}, Hg^{2+} and Pb^{2+} ions, Chem. Eng. J. 395 (2020) 125216.
[15] Y. Wang, T. Nakano, X. Chen, Y.-L. Xu, Y.-J. He, Y.-X. Wu, J.-Q. Zhang, W. Tian, M.-H. Zhou, S.-X. Wang, Studies on adsorption properties of magnetic composite prepared by one-pot method for Cd(II), Pb(II), Hg(II), and As(III): mechanism and practical application in food, J. Hazard. Mater. 466 (2024) 133437.
[16] M. Soylak, A.N. Çoban, H.E.H. Ahmed, Micro solid phase extraction of lead and cadmium using functionalized nanodiamonds@$CuAl_2O_4$@HKUST-1 nanocomposite for FAAS analysis in food and water samples, Food Chem. 442 (2024) 138426.
[17] S.V. Smirnova, T.O. Samarina, D.V. Ilin, I.V. Pletnev, Multielement determination of trace heavy metals in water by microwave-induced plasma atomic emission spectrometry after extraction in unconventional single-salt aqueous biphasic system, Anal. Chem. 90 (2018) 6323–6331.
[18] G. Xing, M.R. Sardar, B. Lin, J.-M. Lin, Analysis of trace metals in water samples using NOBIAS chelate resins by HPLC and ICP-MS, Talanta 204 (2019) 50–56.
[19] C.I. Fort, A. Sanou, M. Coulibaly, K.B. Yao, G.L. Turdean, Green modified electrode for sensitive simultaneous heavy metal ions electrodetection, Sens. Actuat. B Chem. 418 (2024) 136326.
[20] H. Li, R. He, N. Liu, L. Feng, S. Chen, H. Wang, C. Lv, X. Chen, G. Liu, G. Zhao, ZnO/g-C_3N_4 photocatalyst activated by low-pressure ultraviolet for restoring the SWASV signals: a fast pretreatment method for electrochemically detecting Cd^{2+} and Pb^{2+} in soil extracts, Environ. Pollut. 354 (2024) 124183.
[21] R. He, S. Zhang, Y. Shi, C. Lv, J. Wang, N. Liu, W. Ye, X. Wang, G. Liu, G. Zhao, Low-pressure ultraviolet photolysis of soil extracts based on magnetically separable $TiO_2/SiO_2/Fe_3O_4$ photocatalyst for the accurate detection of heavy metals in soil: a new and effective pretreatment method, Microchem. J. 213 (2025) 113646.
[22] R. Huang, J. Lv, J. Chen, Y. Zhu, J. Zhu, T. Wågberg, G. Hu, Three-dimensional porous high boron-nitrogen-doped carbon for the ultrasensitive electrochemical detection of trace heavy metals in food samples, J. Hazard. Mater. 442 (2023) 130020.
[23] W. Gao, H.Y.Y. Nyein, Z. Shahpar, H.M. Fahad, K. Chen, S. Emaminejad, Y. Gao, L.-C. Tai, H. Ota, E. Wu, J. Bullock, Y. Zeng, D.-H. Lien, A. Javey, Wearable microsensor array for multiplexed heavy metal monitoring of body fluids, ACS Sens. 1 (2016) 866–874.
[24] C. Zhang, C. Li, X. Han, Screen printed electrode containing bismuth for the detection of cadmium ion, J. Electroanal. Chem. 933 (2023) 117291.
[25] H. Li, J. Zhao, S. Zhao, G. Cui, Simultaneous determination of trace Pb(II), Cd(II), and Zn(II) using an integrated three-electrode modified with bismuth film, Microchem. J. 168 (2021) 106390.
[26] Q. Bao, G. Li, Z. Yang, P. Pan, J. Liu, J. Chang, J. Wei, L. Lin, Electrochemical performance of a three-layer electrode based on Bi nanoparticles, multi-walled carbon nanotube composites for simultaneous Hg(II) and Cu(II) detection, Chin. Chem. Lett. 31 (2020) 2752–2756.
[27] Z. Wang, Z. Zeng, H. Wang, G. Zeng, P. Xu, R. Xiao, D. Huang, S. Chen, Y. He, C. Zhou, M. Cheng, H. Qin, Bismuth-based metal–organic frameworks and their derivatives: opportunities and challenges, Coordin. Chem. Rev. 439 (2021) 213902.
[28] S.U. Saleem, Y. Liu, J. Sui, G.I.N. Waterhouse, Z. Zhang, L. Yu, Ferrocene-modified bismuth metal-organic framework for ratiometric electrochemical detection of Pb^{2+} and Cu^{2+}, Microchem. J. 213 (2025) 113692.
[29] J. Zou, W. Zhong, F. Gao, X. Tu, S. Chen, X. Huang, X. Wang, L. Lu, Y. Yu, Sensitive electrochemical platform for trace determination of Pb^{2+} based on multilayer Bi-MOFs/reduced graphene oxide films modified electrode, Microchim. Acta 187 (2020) 603–610.
[30] F.-F. Wang, C. Liu, J. Yang, H.-L. Xu, W.-Y. Pei, J.-F. Ma, A sulfur-containing capsule-based metal-organic electrochemical sensor for super-sensitive capture and detection of multiple heavy-metal ions, Chem. Eng. J. 438 (2022) 135639.
[31] X. Han, Y. Shan, H. Zhao, J. Guo, Y. Fu, Y. Zhao, H. Wang, Oxygen vacancy-engineered $NiCo_2O_4$ nanorods/coconut shell biochar hybrids for highly sensitive and selective Pb^{2+} electrochemical detection, Sens. Actuat. B Chem. 446 (2026) 138656.
[32] F. Pan, S. Wei, L. Guggolz, A.R. Eulenstein, F. Tambornino, S. Dehnen, Insights into formation and relationship of multimetallic clusters: on the way toward Bi-rich nanostructures, J. Am. Chem. Soc. 143 (2021) 7176–7188.
[33] M. Ghosh, N. Sepay, D. Schollmeyer, H. Sakiyama, M. Mikuriya, D. Mal, A. Gayen, M.M. Seikh, S. Saha, Spacers directed self-assembly of heterobimetallic copper(II)-lanthanide (III) [Ln = Nd and Gd] moieties: syntheses, structural diversities and magnetic properties, Polyhedron 216 (2022) 115718.
[34] M. Ling, F. Ma, H. Zheng, Z. Yang, Y. Wu, R. Ji, Y. Yu, L. Li, In-situ construction of Bi/$BiVO_4$/Bi–MOF heterostructure with oxygen vacancies: a novel Z-type heterojunction photocatalyst for the degradation of antibiotic, J. Alloy. Compd. 1010 (2025) 177288.

[35] R. Xiong, J. Li, F. Liu, Y. Wu, Y. Xiao, B. Cheng, S. Lei, Interfacial Bi–S chemical bond-coupled sulfur vacancy in Bi_4NbO_8Cl@$ZnIn_2S_{4-x}$S-scheme heterojunction for superior photocatalytic hydrogen generation, J. Colloid Interface Sci. 682 (2025) 690–702.
[36] P.J. Mafa, M.E. Malefane, F. Opoku, A.O. Oladipo, G. Mamba, T.L. Yusuf, J.F. Nure, S.L. Lebelo, D. Liu, J. Gui, B.B. Mamba, A.T. Kuvarega, Dual charge transfer mechanisms in intimately bonded S-scheme heterojunction photocatalyst with expeditious activity toward environmental remediation, Adv. Sust. Syst. 9 (2025) 2401070.
[37] X. Zhang, Y. Zhang, X. Jia, N. Zhang, R. Xia, X. Zhang, Z. Wang, M. Yu, Situ fabrication of a novel S-scheme heterojunction photocatalyts Bi_2O_3/P-C_3N_4 to enhance levofloxacin removal from water, Sep. Purif. Technol. 268 (2021) 118691.
[38] T. Chen, Y. Zou, D. Mao, Y. Bi, Bismuth-based heterometallic clusters capped by thiacalixarene for visible-light photothermal conversion, CrystEngComm 27 (2025) 3528.
[39] V.B. López-Cervantes, J.L. Obeso, J.G. Flores, A. Gutiérrez-Alejandre, R. A. Marquez, J.A. Reyes, C.V. Flores, N.S. Portillo-Vélez, P. Marín-Rosas, C. A. Celaya, E. González-Zamora, D. Solis-Ibarra, R.A. Peralta, I.A. Ibarra, Formation of polysulfides as a smart strategy to selectively detect H_2S in a Bi(iii)-based MOF material, Chem. Sci. 16 (2025) 5483–5492.
[40] G. Lin, B. Zeng, J. Li, Z. Wang, S. Wang, T. Hu, L. Zhang, A systematic review of metal organic frameworks materials for heavy metal removal: synthesis, applications and mechanism, Chem. Eng. J. 460 (2023) 141710.
[41] M. Mansoorianfar, H. Nabipour, F. Pahlevani, Y. Zhao, Z. Hussain, A. Hojjati-Najafabadi, H.Y. Hoang, R. Pei, Recent progress on adsorption of cadmium ions from water systems using metal-organic frameworks (MOFs) as an efficient class of porous materials, Environ. Res. 214 (2022) 114113.
[42] M. Gaberšček, Understanding Li-based battery materials via electrochemical impedance spectroscopy, Nat. Commun. 12 (2021) 6513.
[43] D. Aliyari, M. Mahdavian, B. Ramezanzadeh, Zinc-cobalt bimetallic metal-organic framework (Zn/Co-MOF) nanoparticles as potent pH stimuli anti-corrosive agent for development of a self-healable epoxy composite coating, Mater. Today Chem. 38 (2024) 102105.
[44] V.D. Bui, T.P. Dao, T.H. Vu, V.T. Vu, L. Gnanasekaran, Y. Vasseghian, S.-W. Joo, Ruthenium-doped metal-organic frameworks for green hydrogen generation on a glassy carbon electrode by enhanced electrochemical water splitting, Adv. Compos. Hybrid Mater. 8 (2025) 37.
[45] F. Guo, G. Tian, C. Fan, Z. Zong, J. Wang, J. Xu, A zirconium-organic framework nanosheet-based aptasensor with outstanding electrochemical sensing performance, Inorg. Chem. Commun. 145 (2022) 109970.
[46] W. Wu, J. Wang, D. Luo, Y. Wu, Z. Hu, W. Zhou, Q. Wang, X. You, M. Li, L. Wang, Co_3O_4@carbon nanofiber aerogel electrodes with wide detection range for electrochemical detection of Cd(II) in cigarette butts, J. Environ. Chem. Eng. 13 (2025) 116376.
[47] F. Gholami, M. Roushani, H. Hosseini, Z.M. Karazan, Synthesis of metal-organic framework ZIF-9-Mel and its application as an electrochemical modifier in Pb^{2+} detection, Microchem. J. 201 (2024) 110634.
[48] Q. Ding, C. Li, H. Wang, C. Xu, H. Kuang, Electrochemical detection of heavy metal ions in water, Chem. Commun. 57 (2021) 7215.
[49] U. Ngoensawat, T. Pisuchpen, Y. Sritana-anant, N. Rodthongkum, V.P. Hoven, Conductive electrospun composite fibers based on solid-state polymerized Poly (3,4-ethylenedioxythiophene) for simultaneous electrochemical detection of metal ions, Talanta 241 (2022) 123253.
[50] J. Han, J. Yu, Y. Guo, L. Wang, Y. Song, COFBTLP-1/three-dimensional macroporous carbon electrode for simultaneous electrochemical detection of Cd^{2+}, Pb^{2+}, Cu^{2+} and Hg^{2+}, Sens. Actuat. B Chem. 321 (2020) 128498.
[51] G. Aragay, J. Pons, A. Merkoçi, Recent trends in macro-, micro-, and nanomaterial-based tools and strategies for heavy-metal detection, Chem. Rev. 111 (2011) 3433–3458.
[52] M. Hu, H. He, F. Xiao, C. Liu, Bi-MOF-derived carbon wrapped Bi nanoparticles assembly on flexible graphene paper electrode for electrochemical sensing of multiple heavy metal ions, Nanomaterials 13 (2023) 2069.
[53] Y.-X. Ma, C. Liu, J.-F. Ma, Y. Zhao, A mixed Cd/Cu-based metal-organic framework achieved by postsynthetic metal exchange for electrocatalytic oxidation of uric acid, ACS Mater. Lett. 4 (2023) 2522–2527.
[54] L. Mei, M. Sun, R. Yang, Y. Zhang, Y. Zhang, Z. Zhang, L. Zheng, Y. Chen, Q. Zhang, J. Zhou, Y. Zhu, K.M.Y. Leung, W. Zhang, J. Fan, B. Huang, X.C. Zeng, H.S. Shin, C. Y. Tang, L. Gu, D. Voiry, Z. Zeng, Metallic 1T/1T′ phase TMD nanosheets with enhanced chemisorption sites for ultrahigh-efficiency lead removal, Nat. Common. 15 (2024) 7770.